submitted to *Geophys. J. Int.*

Array-conditioned deconvolution of multiple component teleseismic recordings

C.-W. Chen[1*], D. E. Miller[2], H. A. Djikpesse[2], J. B. U. Haldorsen[2], and S. Rondenay[1]

[1] *Department of Earth, Atmospheric and Planetary Sciences,*

Massachusetts Institute of Technology, Cambridge, MA 02139*, USA. E-mail: cwchen@mit.edu*

[2] *Department of Mathematics and Modeling, Schlumberger-Doll Research, Cambridge, MA* 02139*, USA*

[*] *Now at: Department of Terrestrial Magnetism, Carnegie Institution of Washington, Washington, DC* 20015*, USA*

4 March 2010

SUMMARY

We investigate the applicability of an array-conditioned deconvolution technique, developed for analyzing borehole seismic exploration data, to teleseismic receiver functions and data preprocessing steps for scattered wavefield imaging. This multichannel deconvolution technique constructs an approximate inverse filter to the estimated source signature by solving an overdetermined set of deconvolution equations, using an array of receivers detecting a common source. We find that this technique improves the efficiency and automation of receiver function calculation and data preprocessing workflow. We apply this technique to synthetic experiments and to teleseismic data recorded in a dense array in northern Canada. Our results show that this optimal deconvolution automatically determines and subsequently attenuates the noise from data, enhancing *P*-to-*S* converted phases in seismograms with various noise levels. In this context, the array-conditioned deconvolution presents a new, effective and automatic means for processing large amounts of array data, as it does not require any ad-hoc regularization; the regularization is achieved naturally by using the noise present in the array itself.

Key words: Teleseismic; Multichannel; Deconvolution; Semblance; Optimization.

1 INTRODUCTION

A number of methodologies have been developed over the years to analyze converted seismic waves, ranging from single station applications to high-resolution imaging using dense arrays of broadband seismometers. Such developments have been made possible by the increased availability of teleseismic data recorded at dense broadband seismic arrays. We refer the reader to Rondenay (2009) for a comprehensive review of processing steps that have been developed to obtain images of discontinuities in the Earth's subsurface from data consisting of seismograms sampled by dense arrays of recorders. Of particular interest are methods focused on *P*-to-*S* (*Ps*) conversion in the coda of teleseismic *P* waves, due to its generally high signal-to-noise ratio and lack of contamination from later arriving primary phases. Such signal was first used for direct imaging in landmark studies by Vinnik (1977) and Langston (1979). To increase the signal-to-noise ratio of converted phases, these authors combined records from multiple sources by stacking traces that were source-normalized and time-shifted according to incidence angle. The term receiver function (RF) was introduced by Langston (1979) to describe these normalized records of converted waves and their stacks.

A key step in the RF processing chain is the 'source-normalization', which requires the construction and application of a deconvolution operator to remove the extended earthquake source function, replacing it with an approximate impulse. *The increasing amount of dense array data has motivated the development of new multichannel deconvolution methods, such as simultaneous deconvolution (Bostock & Sacchi 1997), autocorrelation stacking (Li & Nabelek 1999), and pseudostation stacking (Neal & Pavlis 1999, 2001). Here, we examine a multichannel deconvolution method originally developed for analyzing borehole seismic exploration data.* Fig. 1 illustrates this *deconvolution* step using data from the POLARIS-MIT seismic array in the Slave province, Canada. Fig. 1a shows the *P* and *SV* component data from a single earthquake recorded at 18 stations, after application of the free-surface transfer matrix method (Kennett 1991) to partition the three-component records into *P*-*SV*-*SH* wavefields. The effective source function clearly rings for more than a minute, mainly due to reverberation in the crust near the source. Fig. 1b shows the same data after application of a deconvolution operator derived by the method of Haldorsen *et al.*

(1994, 1995), as discussed herein. The deconvolved *SV* data show a clear arrival at ∼4.8 seconds, resulting from *P* to *SV* conversion at the Moho discontinuity. It is the purpose of this paper to discuss this deconvolution method in the context of teleseismic data and to describe its application to data from the POLARIS-MIT array.

2 METHODOLOGIES

Our study focuses on investigating the effectiveness of the array-conditioned deconvolution, in comparison with conventional frequency-domain deconvolution method, i.e., the waterlevel deconvolution. Thus, in this section, we first provide a review of the waterlevel deconvolution method, and then introduce the array-conditioned deconvolution.

2.1 Waterlevel deconvolution

Deconvolution is usually cast as a solution to the forward expression (c.f. Rondenay 2009, Section 5) :

$$d(t) = w(t) * r(t) + n(t) \tag{1}$$

in which the observed signal $d(t)$ is expressed as the convolution of an Earth impulse response $r(t)$ with a source signature $w(t)$. In eq. (1), $n(t)$ represents residual energy, typically assumed to be Gaussian random noise with zero-mean. The normalization process to solve for $r(t)$ involves deconvolving $w(t)$ from $d(t)$. For the ideal case, i.e., there is no noise, the source signature and the observed signal are known and not frequency band-limited, this problem may be solved directly by division in the frequency domain. However, the deconvolution procedure is usually ill-posed because of the presence of random noise, frequency bandwidth limitation, and inaccuracies in estimation of source signature. Therefore, the process has to be regularized. This is usually achieved in the frequency domain by prewhitening the amplitude spectrum of the source wavelet, to avoid small amplitudes that would cause numerical instabilities and ringing in the deconvolved signal.

Hereafter, we will only be using signals in the frequency domain. For simplicity, we shall keep the same notation for the variables in eq. (1).

An approximate solution of the impulse response $\hat{r}$ is expressed as (e.g., Berkhout 1977):

$$\hat{r}(\omega) = \frac{w^*(\omega)}{w(\omega)w^*(\omega) + \delta}\, d(\omega) \tag{2}$$

where the asterisk denotes the complex conjugate, ω is angular frequency and δ is a regularization factor. The factor, sometimes termed waterlevel (Clayton & Wiggins 1976), represents the expected noise power. When δ is zero, eq. (2) is a simple spectral division solving the equation $d(\omega) = w(\omega)\ r(\omega)$. When δ is large, the denominator in eq. (2) is approximately constant and eq. (2) becomes a convolution with the estimated source.

The method assumes that the noise spectrum is white and requires either independent knowledge of the noise power or a search for the 'best' parameter that stabilizes the deconvolution process. This is usually done on a trial and error basis, and thus is subjective and labor-intensive. It is desirable to introduce more objective means to estimate the regularization parameter. For example, Bostock (1998) considered a family of recorded traces $d_m(\omega)$ and associated source estimates $w_m(\omega)$ and proposed choosing δ by minimizing the generalized cross-validation function $GCV(\delta)$ shown as

$$GCV(\delta) = \frac{\sum_{m=1}^{M}\sum_{l=1}^{L}[d_m(\omega_l) - w_m(\omega_l)\hat{r}(\omega_l)]^2}{[ML - \sum_{l=1}^{L} X(\omega_l)]^2}, \tag{3}$$

where

$$X(\omega) = \frac{\sum_{m=1}^{M} w_m(\omega)w_m^*(\omega)}{\sum_{m=1}^{M} w_m(\omega)w_m^*(\omega) + \delta}, \tag{4}$$

with M denoting the number of traces, and L is the number of frequencies represented in the discrete Fourier transform. This process does not require any assumption concerning the noise level in the data, but it still assumes a white noise spectrum and requires an iterative grid search to obtain the value for δ (within a given range) that results in the minimal GCV.

2.2 Array-conditioned deconvolution

Haldorsen *et al.* (1994, 1995) described a method for exploiting the redundancy in seismic array data to obtain an optimized deconvolution filter by using the data to estimate both the source and noise spectra without assuming that either is white. That method may be summarized as follows.

Suppose we are given data recorded at an array of receivers and time-shifted and normalized such that each observed trace $d_m(t)$ can be assumed to contain a common source signature $w(t)$, superposed with a variable 'noise' n_m. That is, we are given a subscripted array of equations, like eq. (1):

$$d_m(t) = w(t) + n_m(t) \tag{5}$$

Here $r(t)$ from eq. (1) is assumed to be an impulse. Thus, all aligned signals contributing to the source estimation are assumed to be part of the source signature. Additional copies shifted and misaligned (e.g., multipath signal arriving obliquely across the array) are formally part of the 'noise', but will be preserved and spiked insofar as they carry the same signature as the aligned signal. Similarly, the filter derived from the aligned *P* data can be applied to *SV* data to compress and enhance the converted signal carrying the same source signature, yielding a compressed arrival with the delay relative to the aligned signal preserved by the deconvolution operator.

In the frequency domain, this data model is written as a set of equations:

$$d_m(\omega) = \hat{w}(\omega) + n_m(\omega). \tag{6}$$

Here we have replaced w with $\hat{w}$ to emphasize the need for an estimate of the signal and the mathematical relationship between the signal estimate $\hat{w}$ and the filter estimate $W(\omega)$ defined as follows. Given an estimate $\hat{w}$ for w, a deconvolution filter W can be determined, independently for each ω, as the solution to the set of eq. (6) *constrained* by the equations

$$W(\omega)d_m(\omega) = 1. \tag{7}$$

These equations have the least-squares solution *(e.g., Press et al. 1992)*

$$W(\omega) = \frac{\hat{w}^*(\omega)}{E_T(\omega)}, \tag{8}$$

where the caret denotes estimate, and $E_T(\omega)$ is the average total energy of the raw traces:

$$E_T(\omega) = \frac{1}{M}\sum_{m=1}^{M} |d_m(\omega)|^2. \tag{9}$$

Substituting d_m *in eq. (9) with the expression in eq. (6)*, eq. (8) can be rewritten as

$$W(\omega) = \frac{\hat{w}^*(\omega)}{|\hat{w}(\omega)|^2 + E_N(\omega)}. \tag{10}$$

where

$$E_N(\omega) = \frac{1}{M}\sum_{m=1}^{M} |d_m(\omega) - w(\omega)|^2. \tag{11}$$

This agrees with eq. (2) when $E_N(\omega)$ is a constant, independent of ω, and thus represents a data-adaptive solution to the filter regularization problem, which is applicable in a wider context than is the waterlevel deconvolution.

The properties of this optimum filter are discussed in detail in Haldorsen *et al.* (1994). *In particular*, one can rearrange eq. (8) to give

$$W(\omega) = \frac{\hat{w}^*(\omega)}{|\hat{w}(\omega)|^2} D(\omega), \tag{12}$$

where the frequency-domain semblance $D(\omega)$ is given by

$$D(\omega) = \frac{|\hat{w}(\omega)|^2}{E_T(\omega)}. \tag{13}$$

The optimum filter in eq. (12) is thus recognized as a spectral division filter, multiplied by the semblance, which acts as a data adaptive, band-limiting filter attenuating frequencies where the signal-to-noise ratio is small.

In the original discussion, the source estimate and the filter construction were derived together, assuming that all the data from a single recorded component were used in constructing both the numerator and the denominator of the filter (eq. (8)). *As noted above, however, these two aspects of the filter construction can be uncoupled and treated separately. Once we have the signature* *estimate $\hat{w}$, the filter obtained by eq.(8) is least-squares optimal for that estimate, independently of how the estimate was obtained.*

Thus, the traces used to estimate $\hat{w}$ may be distinct from those used in estimating E_T. Moreover, the filter itself may be applied to traces that are distinct from the traces used to estimate $\hat{w}$. In particular, when, as in the case of teleseimic data, it may be reasonably assumed that a complicated packet of energy is converted from *P* to *S* somewhere near the receiver array, the *P* arrivals can be aligned and used to estimate the signature while *the complete ensemble of multiple component data* is used in estimating the total energy. Note, however, that stability is only guaranteed if the source estimation traces are included in the estimate for total energy.

In the next section, we carry out synthetic experiments to evaluate the performance of the array-conditioned deconvolution and to compare the results with those using waterlevel deconvolution.

3 SYNTHETIC EXPERIMENTS

We construct the synthetic waveforms by using forward-modeled Earth impulse responses, as well as observed seismograms from the 16 August 2005 earthquake (m_b=6.5) in Japan, recorded at 18 stations of the POLARIS-MIT array in the Slave province, Canada. We perform deconvolution on this synthetic dataset with the addition of various levels of noise. The procedure of the synthetic waveform construction is as follows:

(1) We compute the synthetic *P* and *SV* impulse responses using Zoeppritz reflection and transmission coefficients (e.g., Aki & Richards 2002) calculated for a simple two-layer velocity model and a single horizontal slowness representative of the field data. Fig. 2a shows the result of this computation. The *P* component has the direct *P* wave ($\acute{P}$) and the first order multiples that end with *P* ($\acute{P}\grave{P}\acute{P}$, $\acute{P}\grave{S}\acute{P}$, $\acute{S}\grave{P}\acute{P}$, $\acute{S}\grave{S}\acute{P}$) . The *S* component has the converted *S* wave ($\acute{S}$) and the first order multiples that end with *S* ($\acute{P}\grave{P}\acute{S}$, $\acute{P}\grave{S}\acute{S}$, $\acute{S}\grave{P}\acute{S}$, $\acute{S}\grave{S}\acute{S}$). *Note that the kinematically identical arrivals (e.g. $\acute{P}\grave{S}\acute{S}$ and $\acute{S}\grave{P}\acute{S}$) combine so that there are four arrivals in each mode. Note also* that each *P* arrival has a corresponding *S* arrival obtained by replacing the last *P* segment with an *S* segment, hence the relative time delay is the same in all cases.

(2) We align the *P*-component seismograms of the Japan event and derive a 'synthetic' source

signature through diversity stack (Embree 1968) of the aligned seismograms. *The diversity stack is derived as a least-squares optimal estimate of the signal from aligned traces with constant signal and variable noise (Embree 1968). For each trace, the averaging weight is inversely proportional to the total energy in the trace. For the Slave craton data, we compared the diversity stack with mean, median, and the first eigenvector estimates (Ulrych et al. 1999; Rondenay et al. 2005) and found no significant difference between these methods, except that the median estimate retains more high frequency noise.* This synthetic source signature thus represents the noise-free common source signal (Fig. 2b).

(3) We convolve the synthetic source signal with the synthetic *P* and *SV* impulse responses to yield the noise-free synthetic data (Fig. 2c).

(4) *We extract 300-second long data before the P arrival from each trace of the P- and SV-component seismograms of the Japan event* recorded by the POLARIS-MIT array, to be representative of background noise. We also subtract the synthetic source signal from the respective observed *P*-component seismogram, and the residuals obtained are representative of additional incoherent noise between traces. We combine these two types of noise, randomly shift them in the time domain, and add a scaling factor λ for controling the amplitude, before adding them to the noise-free synthetic data. As such, *we generate synthetic seismograms with characteristics of an actual earthquake and actual noise variations across an array.* The complete synthetic data model for the *P*-component ($d_p(t)$) and *SV*-component ($d_{sv}(t)$) can be thus described as, respectively,

$$d_p(t) = \hat{w}(t) * g_p(t) + \lambda N_p(t); \tag{14}$$

and

$$d_{sv}(t) = \hat{w}(t) * g_{sv}(t) + \lambda N_{sv}(t), \tag{15}$$

where $g_p(t)$ and $g_{sv}(t)$ are the synthetic *P* and *SV* impulse responses, and $N_p(t)$ and $N_{sv}(t)$ are the total (combined and shifted) noise in *P* and *SV* components. By changing the scaling factor λ, we are able to generate synthetic data with various noise levels so as to test the effectiveness of the deconvolution methods. *Note that λ does not change the spectral content of the noise.*

Fig. 3 summarizes the results of the synthetic experiments. Fig. 3a shows the synthetic array data (*P* and *SV* components) with noise level λ=1. Fig. 3b and 3c show the deconvolution results using the waterlevel method with the GCV-derived δ parameter and with waterlevel of 1% of the maximum amplitude of the source signature estimate, respectively. Fig. 3d shows the result using the array deconvolution. This synthetic test allows us to make the following observations. First, the GCV yields trace-dependent δ values that are equivalent to 0.001 to 0.01 percent of the maximum amplitude of the source estimate. Second, while the waterlevel method in general recovers the impulse response in most *SV* traces, it fails to resolve traces that are anomalously noisy, for instance, traces 3 and 17. Furthermore, as the waterlevel factor increases, the deconvolved signal broadens and loses resolution. This is expected because using a higher waterlevel amounts to prewhitening more high frequency signals. In a sense, it becomes a low-pass filter, removing high frequency content in the data. Conventionally, this process of iterating over a number of waterlevel factors is conducted and visual inspection is required until a 'best' waterlevel is determined. On the other hand, the array deconvolution (Fig. 3d) does not require any iterative process or human intervention, and stabilizes noisy traces while better resolving the impulse response consistently across the array. Here, $E_T(\omega)$ is calculated using *P*-component data.

Note that, in the deconvolution process, $\hat{w}(t)*g_p(t)$ becomes the effective source signature, and that relative amplitudes in the deconvolved *SV* data are slightly altered from those of $g_{sv}(t)$. This is an issue for any deconvolution process. The consistency achieved by using a single deconvolution operator for all receivers should enable further analysis beyond the scope of this paper.

Similar results are observed when we increase the noise in the synthetic data. The waterlevel deconvolution becomes unstable, i.e., the deconvolved traces are more ringing, whereas the array deconvolution still achieves similar resolution.

One way to evaluate the performance of the deconvolution filters is to measure the variance between the deconvolved signals across the array. We calculate the variance by summing the square of the difference between each trace and the mean trace. The corresponding variance of each deconvolved data section is shown as the number in the parentheses above each panel in Fig. 3. The array deconvolution yields a much better, i.e., smaller, variance than those from the other two approaches. For waterlevel deconvolution, we note that there appears to be a trade-off between variance and broadening of the deconvolved signal; larger waterlevel results in smaller variance but less sharp impulse. *The choice of the optimal waterlevel is thus based on this trade-off: when increasing waterlevel beyond a certain value does not reduce the variance significantly, we designate this value as the optimal waterlevel to use (1% in this synthetic case).* In contrast, array-coditioned deconvolution always achieves small variance and sharper impulse. *Fig. 4 shows the comparison of the amplitude spectra of deconvolved signals of trace 3 (Fig. 3) derived from the array approach and the waterlevel approach, respectively, along with the amplitude spectrum of the raw synthetic trace. The spectra are normalized by the amplitude at 0.5 Hz of each trace. The raw synthetic data is dominated by low frequency noise, and the array deconvolution, compared with the waterlevel method, achieves a better resolution of the impulse without sacrificing much higher frequency (0.5-1.5 Hz) content. We emphasize that, since array deconvolution estimates a different noise energy for each frequency whereas waterlevel deconvolution uses a single noise parameter for all frequencies, the difference between array deconvolution and optimal waterlevel deconvolution is most significant when the source time function and/or noise is not spectrally flat. In particular, this is true when the signature contains near-source reverberation.*

In this section, we have demonstrated the effectiveness of the array-conditioned deconvolution, especially for noisy data. In the following section, we will apply this deconvolution to a field dataset of the Slave province. In this example, We focus our demonstration on the *P*- and *SV*-component seismograms, but note that the method is readily applicable to *SH* components as well.

4 APPLICATION TO THE SLAVE CRATON ARRAY DATA

We use seismic array data recorded in the Slave province, an Archean craton which is located in the northwestern Canadian Shield. The Slave craton has been the subject of intensive geophysical and petrological studies due to its longevity and the presence of abundant diamondiferous kimberlites. The POLARIS-MIT seismic array (Fig. 5a) in the Slave craton consists of 30 seismic stations, each equipped with a three-component broadband seismometer. A previous receiver-function study (Chen *et al.* 2009) identified a distinct crust-mantle boundary, or Moho, at $\sim$4.8

s across the array, using waterlevel deconvolution and common-conversion-depth stacks of high quality data from 62 teleseismic events with magnitude $m_b \geq 5.8$ recorded during 2004-2006. Now, using the new array-conditioned deconvolution method, we are able to analyze data from 135 events with magnitude $m_b \geq 5.5$ (Fig. 5a) during the same recording period. We use the event locations provided by the USGS PDE catalog, and rotate the horizontal-component data to radial and transverse components (vertical component remains the same). We subsequently partition the components into *P*, *SV*, and *SH* wavefields by the free surface transfer matrix (Kennett 1991). After wavefield partition, we align the data by the predicted arrival times calculated in a 1-D global reference model (e.g., iasp91, Kennett & Engdahl 1991). The source signature is estimated from the *P*-component by diversity stack (Embree 1968), and the noise energy is calculated from the *P*-component data. The deconvolution is then performed to yield deconvolved *P* and *S* signals. We observe that the deconvolved *P* impulses across the array often show time differences between each other, indicating inaccurate original reference alignment. Therefore, in practice, the deconvolved *P* impulses are iteratively realigned by adjusting their time lags, and a subsequent deconvolution is performed to yield the final results.

Fig. 6 shows the raw data of four example earthquakes. These raw data show different characteristics of the coherently aligned signals in the *P* components, marking the various earthquake source signatures, as well as different patterns and amplitudes of the background noise in the *SV* components. Fig. 7 shows their deconvolved results from array deconvolution, compared with those from waterlevel deconvolution. The results of earthquake data are consistent with those of synthetic tests. Both deconvolution methods result in delta-function-like and well-aligned *P* signals; however, the array-deconvolved ones appear sharper, indicating the effectiveness of the array deconvolution in collapsing the signal into a spike. On the *SV* components, coherent signals at $\sim$4.8 s can be observed in all data sections, representing the conversion at the Moho. However, the array-deconvolved data appear more stable and consistent throughout, while the corresponding waterlevel-deconvolved data are less so. In addition, a number of differences are worth noting. First, the array-deconvolved traces contain more high frequency energy than do the waterlevel-deconvolved ones. Second, there are traces that cannot be well resolved by waterlevel deconvolution and that result in anomalously low frequency signal (e.g., in the Costa Rica event, *SV* traces 1 and 8; in the Tonga event, traces 3, 6, and 8). In contrast, array deconvolution in general achieves more stability. We also calculate the variance, as defined in the synthetic tests, of the deconvolved data (shown as the number in the parentheses above each panel). In these four examples, the array-deconvolved data all have much smaller variances (at least one order of magnitude smaller) than those of the waterlevel-deconvolved ones. This shows the advantage of array deconvolution in extracting coherent signals across array while attenuating noise. An additional advantage can be noted by examining the Tonga event (Fig. 7d). This event has a magnitude m_b = 6.3, but the noisy *SV* components with anomalous low frequency patches has prevented it from being used in the previous receiver function analysis. Using the array deconvolution, however, we are able to attain more stable and thus usable signals from this event.

Of course, additional tweaking of the waterlevel processing, e.g by highpass filtering of noisy traces could reduce the difference between the waterlevel and array-derived results. The main point of this paper is that such expert tweaking can be largely replaced by an automated process suitable for treating very large data sets including data with very low signal-to-noise ratios.

The processing procedure is implemented for the whole dataset of 135 events. In Fig. 8, we show the deconvolved *SV* traces as a function of backazimuth at five receivers. We observe that, in addition to coherent signals corresponding to the Moho, there appears to be various coherent signals at different times between the surface $(t = 0s)$ and the Moho $(t = 4.8s)$ from receiver to receiver. These variations suggest the presence of local crustal heterogeneities beneath each receiver, and were not observed before when only limited high quality seismic records were utilized. We also plot the deconvolved data as a function of earthquake magnitude. An example using data from station ACKN is shown in Fig. 9. We observe that the Moho signal appears consistently visible in the entire magnitude range, and does not degrade at smaller magnitudes (5.5 $\leq m_b <$ 5.8). *This means that the noise for these records is primarily signal-generated, consisting mainly of misaligned scattered energy (which is preserved and deconvolved insofar as it shares a signature with the direct signal) and residual energy not captured by the source estimate (due, e.g. to variable receiver response and errors in the polarization preprocessing). The data used for this* *study were selected before the results were known and it seems clear that the pre-selection process was excessively restrictive and* that the array deconvolution can be readily applied to earthquakes with smaller magnitudes. Further analysis of this application is the topic of a separate paper.

In closing, we note that, traditionally, the deconvolution has been achieved in an iterative manner, whether it is to find a 'best' regularization parameter in the frequency-domain deconvolution, or to minimize the difference between observed and modeled data in the time-domain deconvolution (e.g., Gurrola *et al.* 1995; Liggoría & Ammon 1999). In this context, the array-conditioned deconvolution presents a new, effective and automatic means for processing large amounts of array data, as it does not require any ad-hoc regularization; the regularization is achieved naturally by using the noise present in the array itself.

5 CONCLUSIONS

The application of the array-conditioned deconvolution improves the efficiency and automation of the deconvolution process that is an essential step in receiver function analysis and in data preprocessing for imaging of scattered waves. Synthetic experiments demonstrate the effectiveness of the deconvolution technique, especially for noisy data. Application of this technique to a teleseismic dataset from the Slave craton yields a deconvolved data section that clearly identifies the *Ps* conversion at the Moho, and suggests the presence of local crustal heterogeneities beneath each receiver. The performance of the array deconvolution with noisy data promises the potential of exploiting earthquakes with smaller magnitudes, which would increase the number of usable sources, thus providing more comprehensive azimuthal coverage than was possible before.

ACKNOWLEDGMENTS

We thank Gary Pavlis and an anonymous reviewer for their thoughtful comments that helped improve the clarity of this manuscript. This work was initiated and mostly carried out during a summer internship of C.-W. Chen at Schlumberger-Doll Research in 2008. The POLARIS-MIT array data were collected and analyzed as part of the Slave craton experiment, which was funded by the POLARIS consortium and the US National Science Foundation grant EAR-0409509 to S. Rondenay.

REFERENCES

Aki, K. & Richards, P.G., 2002. *Quantitative Seismology*, 2nd Ed., University Science Books.

Berkhout, A.J., 1977. Least-squares inverse filtering and wavelet deconvolution, *Geophysics*, **42**, 1369-1383.

Bleeker, W., Ketchum, L., Jackson, V. & Villeneuve, M., 1999. The central Slave basement complex, part I: its structural topology and autochthonous cover, *Can. J. Earth Sci.*, **36**, 1083-1109.

Bostock, M.G., 1998. Mantle stratigraphy and evolution of the Slave province, *J. geophy. Res.*, **103**, 21183-21200.

Bostock, M.G. & Sacchi, M.D., 1997. Deconvolution of teleseismic recordings for mantle structure, *Geophys. J. Int.*, **129**, 143-152.

Chen, C.-W., Rondenay, S., Evans, R.L. & Snyder, D.B., 2009. Geophysical detection of relict metasomatism from an Archean ($\sim$3.5 Ga) subduction zone, *Science*, **326**, 1089-1091.

Clayton, R.W. & Wiggins, R.A., 1976. Souce shape estimation and deconvolution of teleseismic bodywaves, *Geophys. J. R. astr. Soc.*, **47**, 151-177.

Embree, P., 1968. Diversity seismic record stacking method and system, *U.S. Patent*, **3,398,396**.

Gurrola, H., Baker, G.E. & Minster, J.B., 1995. Simultaneous time-domain deconvolution with application to the computation of receiver functions, *Geophys. J. Int.*, **120**, 537-543.

Haldorsen, J.B.U., Miller, D.E. & Walsh, J.J., 1994. Multichannel Wiener deconvolution of vertical seismic profiles, *Geophysics*, **59**, 1500-1511.

Haldorsen, J.B.U., Miller, D.E. & Walsh, J.J., 1995. Walk-away VSP using drill noise as a source, *Geophysics*, **60**, 978-997.

Kennett, B.L.N., 1991 The removal of free surface interactions from three-component seismograms, *Geophys. J. Int.*, **104**, 153-163.

Kennett, B.L.N. & Engdahl, E.R., 1991. Traveltimes for global earthquake location and phase identification, *Geophys. J. Int.*, **105**, 429-465.

Langston, C., 1979. Structure under Mount Rainier, Washington, inferred from teleseismic body waves, *J. geophy. Res.*, **84**, 4749-4762.

Li, X.-Q. & Nábělek, J.L., 1999. Deconvolution of teleseismic body waves for enhancing structure beneath a seismometer array, *Bull. Seis. Soc. Am.*, **89**, 190-201.

Ligorría, J.P, Ammon, C.J., 1999. Iterative deconvolution and receiver-function estimation, *Bull. Seismol. Soc. Am.*, **89**, 1395-1400.

Neal, S.L. & Pavlis, G.L., 1999. Imaging *P*-to-*S* conversions with multichannel receiver functions, *Geophys. Res. Lett.*, **26**, 2581-2584.

Neal, S.L. & Pavlis, G.L., 2001. Imaging *P*-to-*S* conversions with broad-band seismic arrays using multichannel time-domain deconvolution, *Geophys. J. Int.*, **147**, 57-67.

Press, W.H., Teukolsky, S.A., Vetterling, W.T. & Flannery, B.P., 1992. *Numerical Recipes*, 2nd Ed., Cambridge University Press, 992 pp.

Rondenay, S., Bostock, M.G. & Fischer, K.M., 2005. Multichannel inversion of scattered teleseismic body waves: Practical considerations *Seismic Earth: Array analysis of broadband seismograms*, edited by Levander A. & Nolet G., AGU Geophysical Monograph Series, **157**, 187-204.

Rondenay, S., 2009. Upper mantle imaging with array recordings of converted and scattered teleseismic waves, *Surv. Geophys.*, in press, doi:10.1007/s10712-009-9071-5.

Ulrych, T.J., Sacchi, M.D. & Freire, S.L.M., 1999. Eigenimage processing of seismic sections, in *Covariance Analysis for Seismic Signal Processing, Geophys. Development*, **8**, Soc. Exploration Geophysicists, 978-997.

Vinnik, L.P., 1977. Detection of waves converted from *P* to *SV* in the mantle, *Phys. Earth Planet. Inter.*, **15**, 39-45.

Table 1. The earthquake parameters of the four exemplary events. Δ is epicentral distance from the event to the center of the POLARIS-MIT array. Baz is backazimuth of the event with respect to the array, counting clockwise from north.

Date	Time	Latitude (°N)	Longitude (°E)	Depth (km)	m_b	Δ (°)	Baz (°)	Location
2004/01/25(025)	11:43:11	-16.83	-174.196	129.8	6.4	94.5959	239.3742	Tonga Islands
2004/03/17(077)	05:21:00	34.589	23.326	24.5	5.9	74.3788	38.0443	Crete, Greece
2004/06/29(181)	07:01:30	10.738	-87.043	9	5.8	56.3828	151.9377	Costa Rica
2005/08/16(228)	02:46:28	38.276	142.039	36	6.5	62.6444	302.5049	Honshu, Japan

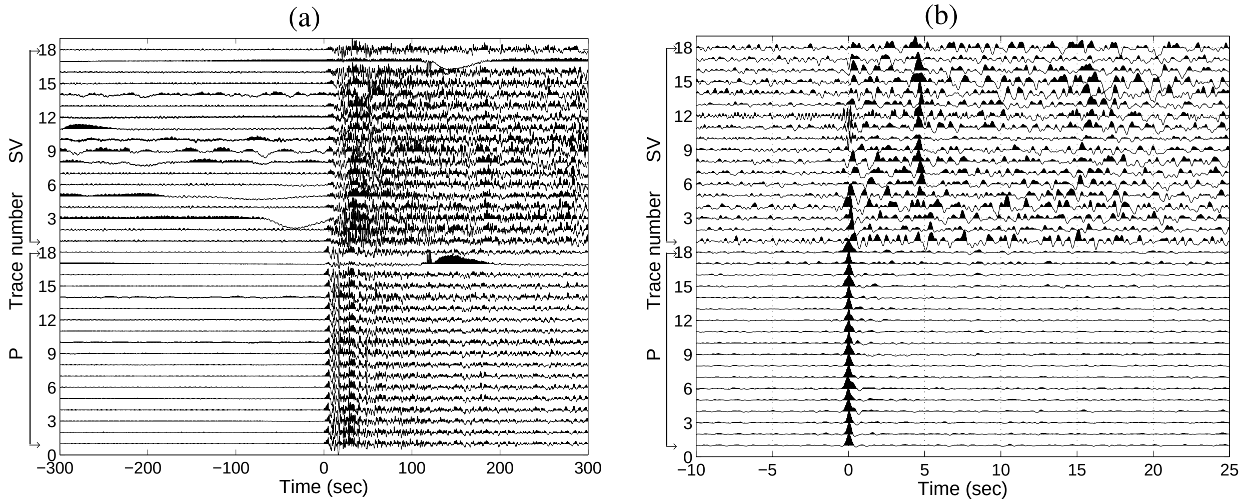

Figure 1. (a) The *P*- and *SV*-component data of a Japan (m_b=6.5, 36-km deep) earthquake. (b) The deconvolved *P*- and *SV*-component data of (a).

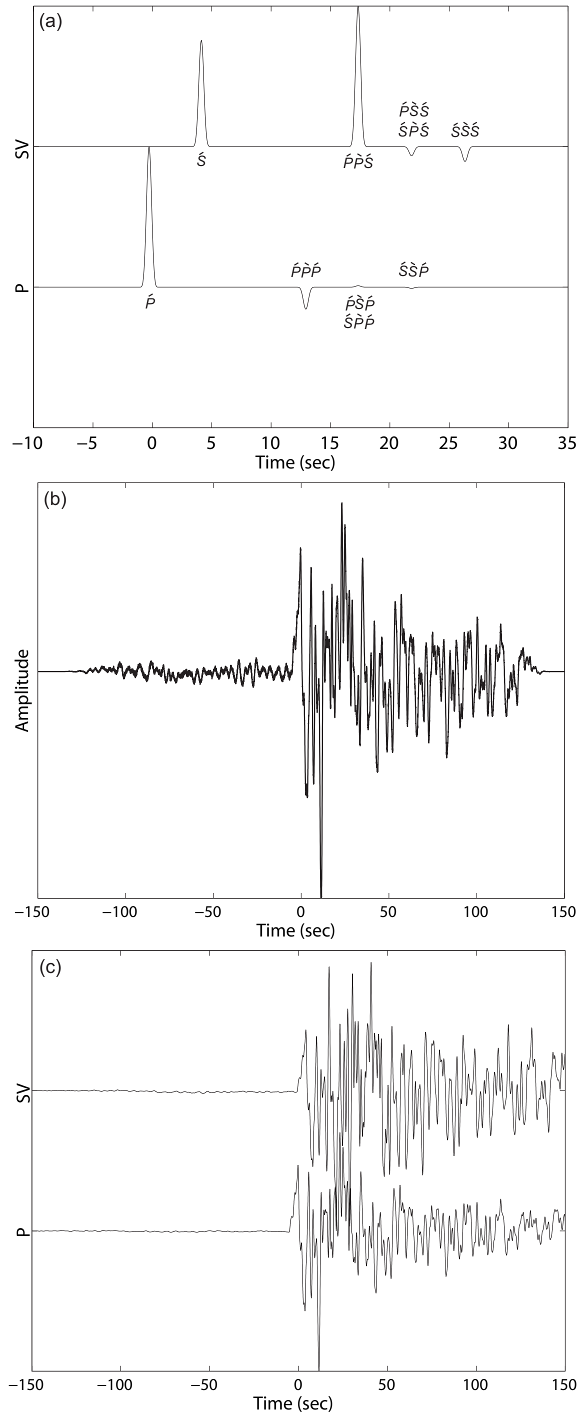

Figure 2. (a) The synthetic P- and SV-component impulse responses for an incident P wave of ray parameter p=0.06 s/km, sampling an isotropic two-layer model. The model cosists of a 40 km-thick horizontal layer (α_0=6.6 km/s, β_0=3.7 km/s, ρ_0=2600 kg/m^3) over a half space (α_1=8.1 km/s, β_1=4.5 km/s, ρ_0=3500 kg/m^3). (b) The source signature estimate used to construct the synthetic array data. (c) The noise-free synthetic data constructed from convolving (a) with (b).

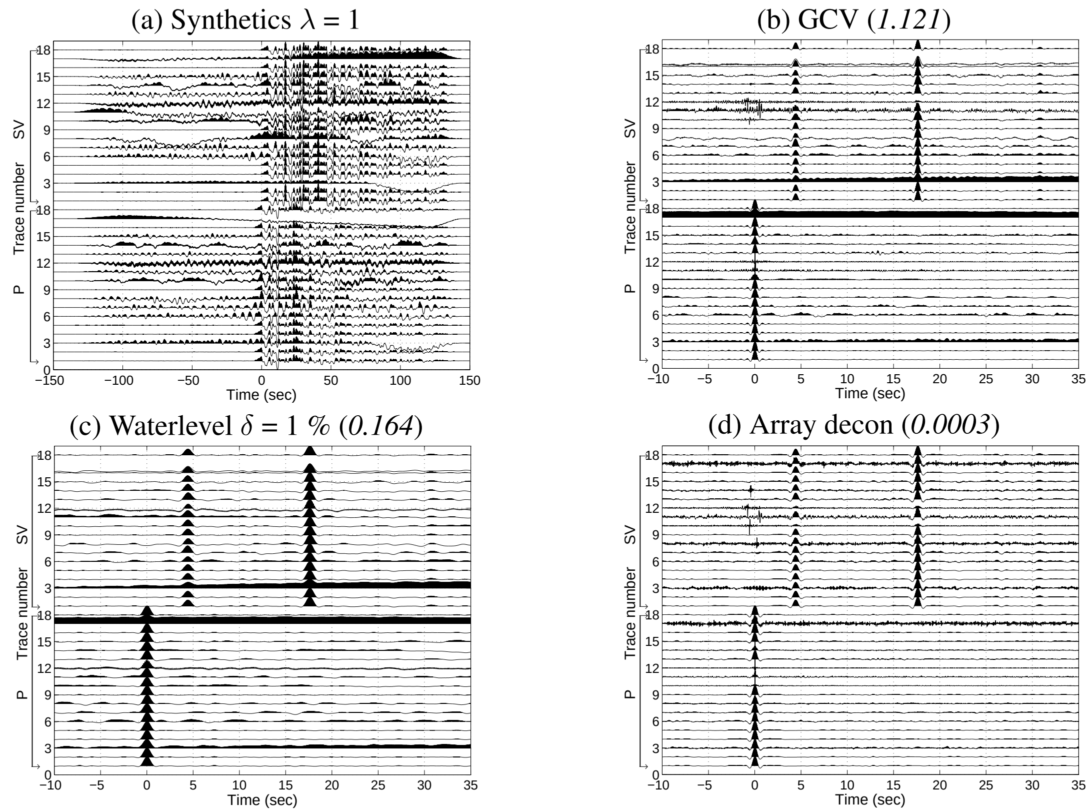

Figure 3. Summary of the synthetic experiments. (a) The synthetic array data of λ=1. The deconvolved data section using (b) waterlevel deconvolution with GCV-derived δ; (c) waterlevel deconvolution with the factor of 1%; and (d) array-conditioned deconvolution. The number in the parentheses indicates the corresponding variance.

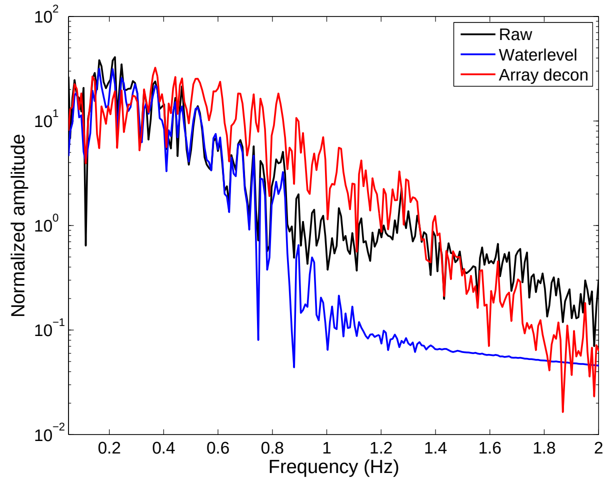

Figure 4. Comparison of the amplitude spectra of the deconvolved *SV* signals of trace 3, derived from the array deconvolution and the waterlevel deconvolution, respectively. The amplitude spectrum of the 'raw' synthetic trace is also plotted. The spectra are normalized by the amplitude at 0.5 Hz of each trace. Note that the spectra have been decimated by a factor of 5.

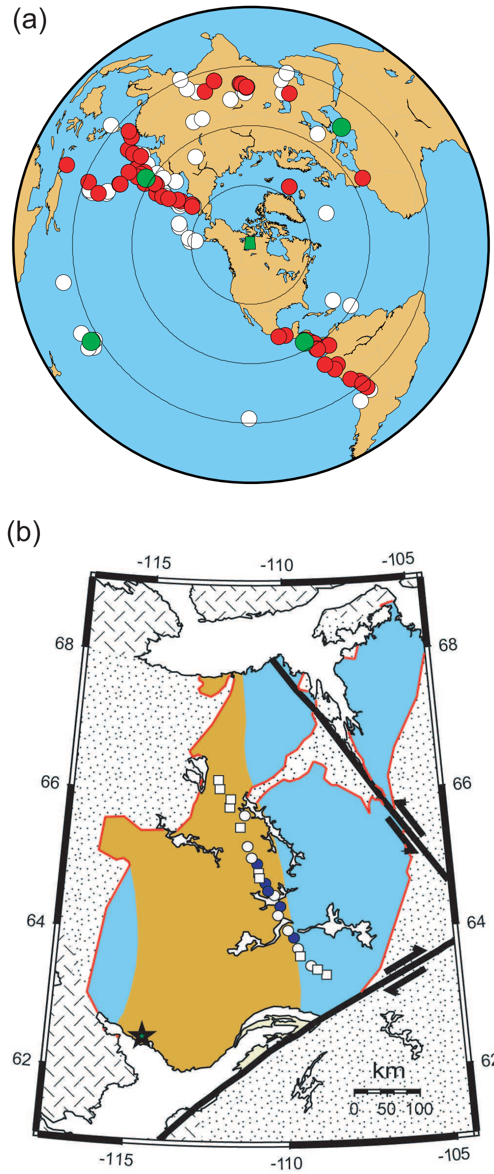

Figure 5. (a) The earthquake event distribution projected with the Slave craton in the center (green square). The red circles denote events used in the previous receiver function study (Chen *et al.* 2009). The white circles denote the additional events that are analyzed by the array deconvolution. The green circles denote the four exemplary events whose data are shown in Fig. 6. The combined dataset includes a total of 135 events. (b) Simplified geological map of the Slave craton (outlined in red). The brown shaded area is the central Slave basement complex (CSBC; Bleeker *et al.*, 1999), which is the oldest portion (2.6-4 Ga) of the craton. The blue shaded area denotes the eastern Slave craton where is covered by juvenile crust. The seismic stations used in this study are denoted in squares (MIT stations) and circles (POLARIS stations). The five stations denoted in blue are those whose data are shown in Fig. 8. From south to north, these stations are BOXN, LGSN, LDGN, EKTN, and ACKN.

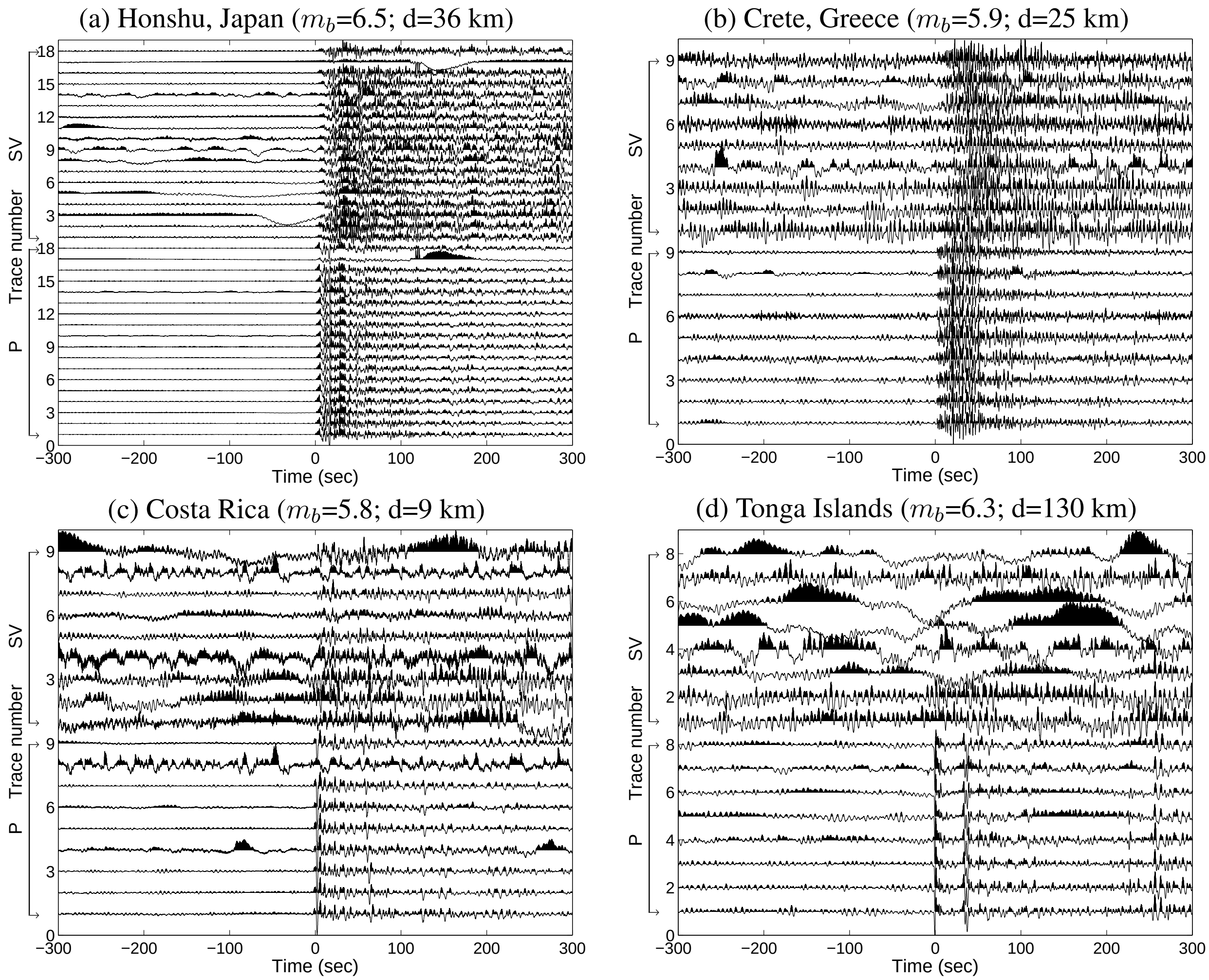

Figure 6. The raw data (*P* and *SV* components) of four exemplary earthquakes from (a) Honshu, Japan; (b) Crete, Greece; (c) Costa Rica; and (d) Tonga Islands. Note the traces are individually normalized. The magnitude (m_b) and depth associated with each event are also indicated.

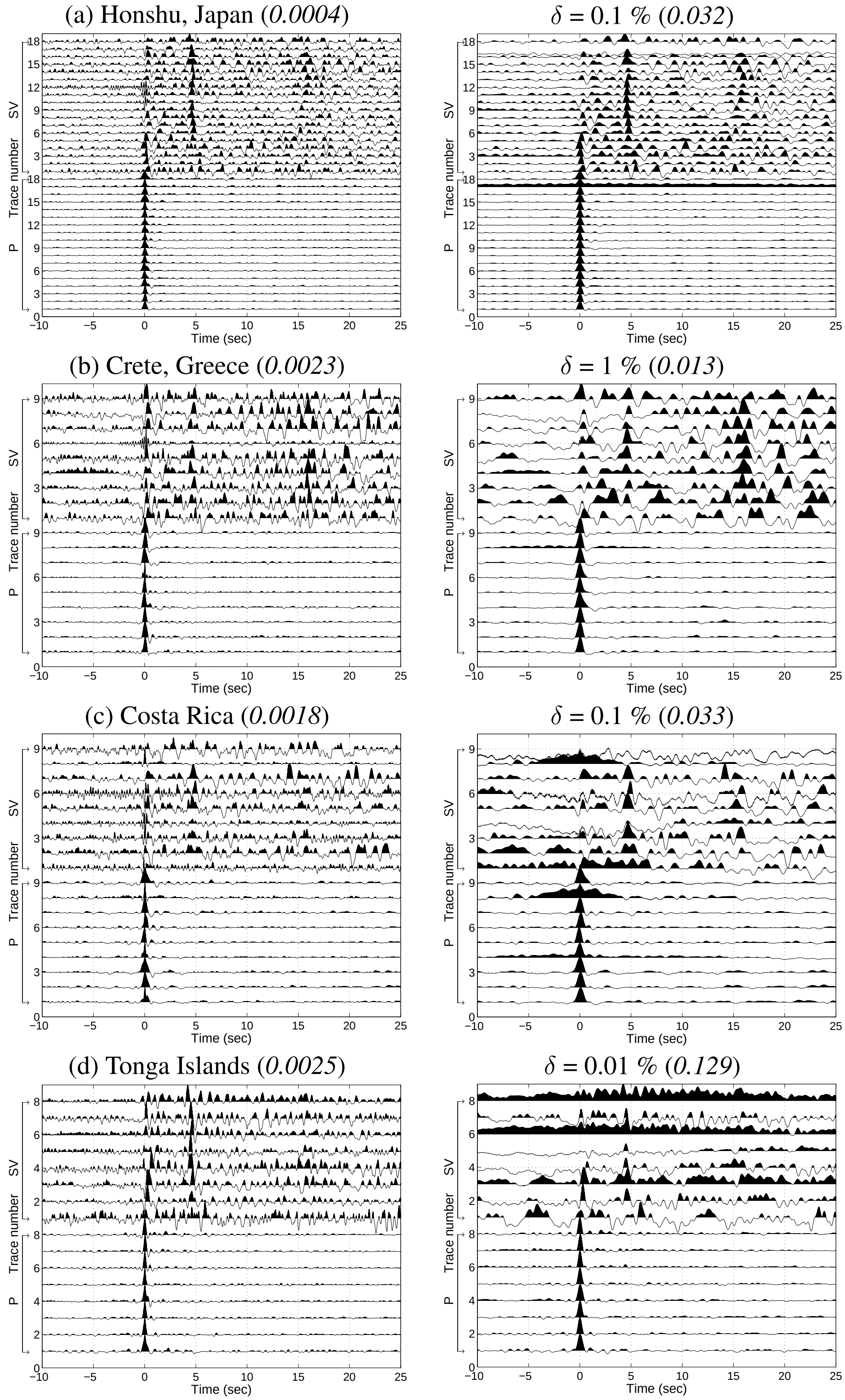

Figure 7. The deconvolved data of the four earthquakes shown in Fig. 6. The left column shows the results from array-conditioned deconvolution. The right column shows the corresponding results from waterlevel deconvolution, denoted with the waterlevel factor used. *The choice of waterlevel is based on the trade-off between the variance and the broadening of the signal.* The number in the parentheses indicates the corresponding variance.

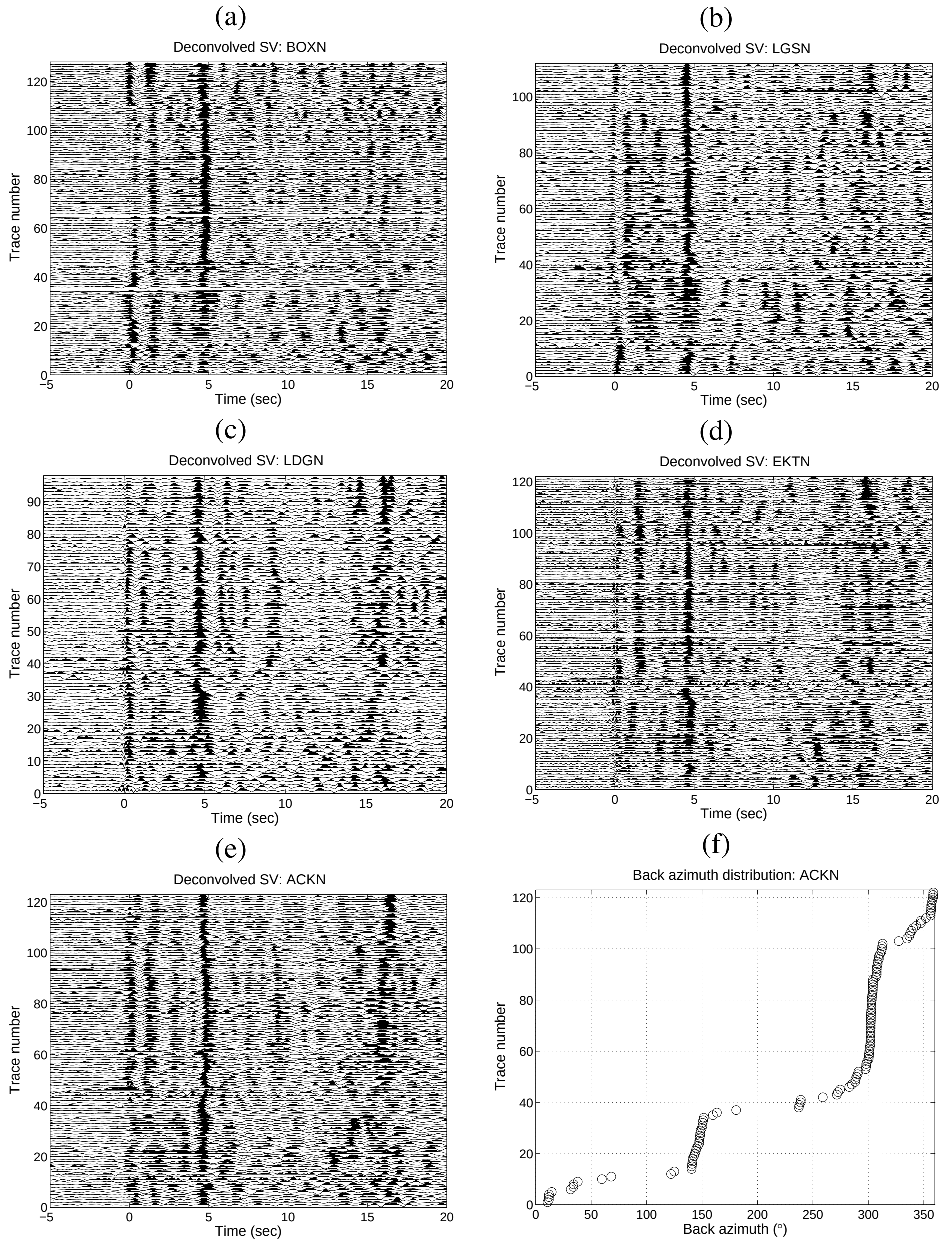

Figure 8. The deconvolved *SV* data sections of five receivers. (a) BOXN; (b) LGSN; (c) LDGN; (d) EKTN; (e) ACKN. (f) The representative backazimuthal distribution of the teleseismic events recorded at this array. A majority of earthquakes are located at the western Pacific subduction zones (around 300°).

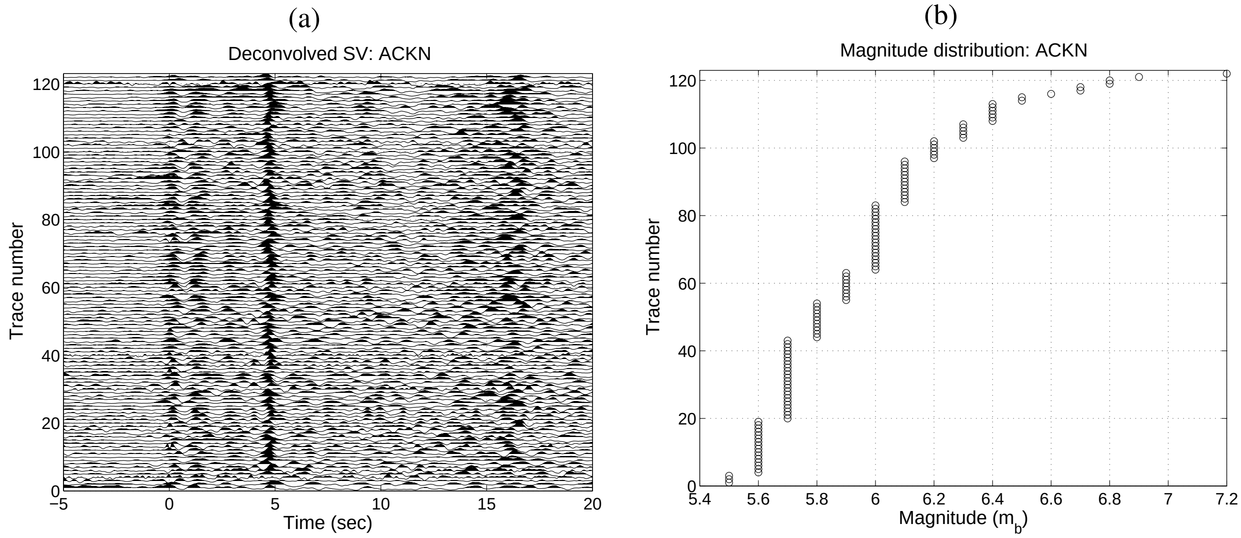

Figure 9. (a) The deconvolved *SV* data section of station ACKN plotted as a function of earthquake magnitude. (b) The distribution of traces according to magnitude.

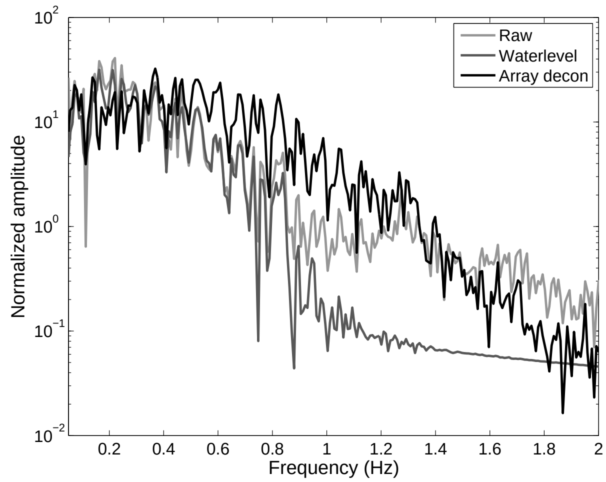

Figure 4. Comparison of the amplitude spectra of the deconvolved *SV* signals of trace 3, derived from the array deconvolution and the waterlevel deconvolution, respectively. The amplitude spectrum of the 'raw' synthetic trace is also plotted. The spectra are normalized by the amplitude at 0.5 Hz of each trace. Note that the spectra have been decimated by a factor of 5.

(a)

(b)

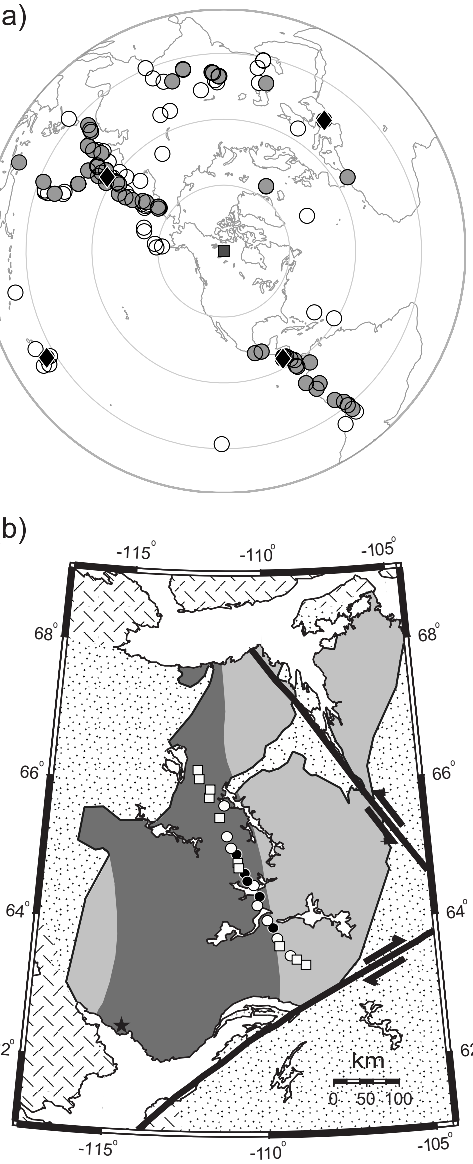

Figure 5. (a) The earthquake event distribution projected with the Slave craton in the center (gray square). The gray circles denote events used in the previous receiver function study (Chen *et al.* 2009). The white circles denote the additional events that are analyzed by the array deconvolution. The black diamonds denote the four exemplary events whose data are shown in Fig. 6. The combined dataset includes a total of 135 events. (b) Simplified geological map of the Slave craton (outlined in red). The dark gray shaded area is the central Slave basement complex (CSBC; Bleeker *et al.*, 1999), which is the oldest portion (2.6-4 Ga) of the craton. The light gray shaded area denotes the eastern Slave craton where is covered by juvenile crust. The seismic stations used in this study are denoted in squares (MIT stations) and circles (POLARIS stations). The five stations denoted in black are those whose data are shown in Fig. 8. From south to north, these stations are BOXN, LGSN, LDGN, EKTN, and ACKN.